Synthesis of Monodisperse TiO_2—Paraffin Core—Shell Nanoparticles for Improved Dielectric Properties

Balamurugan Balasubramanian,* Kristin L. Kraemer, Nicholas A. Reding, Ralph Skomski, Stephen Ducharme, and David J. Sellmyer

Nebraska Center for Materials and Nanoscience and Department of Physics and Astronomy, University of Nebraska, Lincoln, Nebraska 68588

ABSTRACT Core—shell structures of oxide nanoparticles having a high dielectric constant, and organic shells with large breakdown field are attractive candidates for large electrical energy storage applications. A high growth temperature, however, is required to obtain the dielectric oxide nanoparticles, which affects the process of core—shell formation and also leads to poor control of size, shape, and size-distribution. In this communication, we report a new synthetic process to grow core—shell nanoparticles by means of an experimental method that can be easily adapted to synthesize core—shell structures from a variety of inorganic—organic or inorganic—inorganic materials. Monodisperse and spherical TiO_2 nanoparticles were produced at room temperature as a collimated cluster beam in the gas phase using a cluster-deposition source and subsequently coated with uniform paraffin nanoshells using *in situ* thermal evaporation, prior to deposition on substrates for further characterization and device processing. The paraffin nanoshells prevent the TiO_2 nanoparticles from contacting each other and also act as a matrix in which the volume fraction of TiO_2 nanoparticles was varied by controlling the thickness of the nanoshells. Parallel-plate capacitors were fabricated using dielectric core—shell nanoparticles having different shell thicknesses. With respect to the bulk paraffin, the effective dielectric constant of TiO_2—paraffin core—shell nanoparticles is greatly enhanced with a decrease in the shell thickness. The capacitors show a minimum dielectric dispersion and low dielectric losses in the frequency range of 100 Hz—1 MHz, which are highly desirable for exploiting these core—shell nanoparticles for potential applications.

KEYWORDS: core—shell nanoparticles · cluster-deposition · capacitors · dielectric properties

Hybrid nanostructures, such as core—shell nanoparticles, are fascinating owing to new physical phenomena involved in these structures, which can be exploited for optical, electrical, magnetic, and biological applications.[1−5] The core—shell formation of two materials, however, is mostly driven by the reaction environment and a significant difference in their atomic sizes and surface energies. The preferential surface segregation of the material having relatively large atomic size and low surface energy leads to the spontaneous formation of core—shell structures.[2,3,6] Wet chemical techniques have been used to grow hybrid core—shell nanoparticles by functionalizing inorganic nanoparticles with organic molecules, but require complicated and multistep processes: the growth of inorganic nanoparticles, attachment of suitable cross-linkers through which the organic molecules can be functionalized with the nanoparticle surface, and finally the deposition of these core—shell nanoparticles on suitable substrates for device fabrication.[4,7−9] In addition, certain inorganic nanoparticles, such as dielectric oxide nanoparticles, require high-temperature growth,[10−13] which is expected to make the core—shell formation process difficult and also leads to poor control in shape, size, and size-distribution. In this communication, we report the synthesis of monodisperse core—shell nanoparticles, for example TiO_2—paraffin, by means of a hybrid experimental method consisting of a plasma-condensation-type cluster-deposition to produce TiO_2 nanoparticles at room temperature, followed by an *in situ* thermal evaporation of paraffin to form uniform nanoshell coatings on the surface of oxide nanoparticles.

Recently, nanocomposites in which oxide nanoparticles having high dielectric constant (k) dispersed in an organic matrix with high breakdown field (E_b) have emerged as attractive candidates for large electrical energy storage,[14−20] which is required for mobile electronic devices, hybrid electric vehicles, and stationary power systems.[21−23] While batteries are used almost exclusively in these applications, high-energy-density capacitors are showing great promise.[22,23] At present, various organic materials such as paraffin, polyethylene, polystyrene, and certain ferroelectric polymers are used as dielectrics in

*Address correspondence to bbalasubramanian2@unl.edu.

Received for review November 17, 2009 and accepted March 19, 2010.

Published online April 1, 2010.
10.1021/nn9016422

capacitors due to their large E_b.[23,24] The maximum energy stored in these capacitors ($U_{max} = 0.5\varepsilon_0 k E_b^2$), however, is limited due to their relatively low k, typically less than 10.[24] High dielectric constants and energy densities have been attained with relaxor terpolymers based on polyvinylidene fluoride (PVDF).[25−27] Similarly, the effective dielectric constant of above-mentioned organic materials can be enhanced by embedding oxide nanoparticles, such as TiO_2, $SrTiO_3$, $BaTiO_3$, and $BaSrTiO_3$, which have dielectric constants varying from a few tens to several thousands depending on their stoichiometry and crystal structure.[14−18]

A high-temperature growth or postdeposition heat treatment at more than 400 °C, however, is required to obtain crystalline oxide nanoparticles in contrast to the low melting point and decomposition temperature of organic materials, typically less than 300 °C depending on their structural units.[10−13,28] Thus, wet chemical techniques have been adapted to fabricate nanocomposites by simply mixing the commercially available oxide nanoparticles of much bigger sizes (*ca.* 30 −70 nm) with organic materials.[14−18] A major impediment, however, is poor control of the size and size-distribution of the nanoparticles and their tendency to agglomerate even at a relatively low loading of 10 vol % in an organic matrix, leading to poor film quality and device characteristics.[11,12] In the present study, TiO_2 nanoparticles of much smaller sizes of around 10 nm were produced in the gas phase and were coated with uniform paraffin nanoshells, prior to deposition on substrates. The paraffin nanoshells prevent the TiO_2 nanoparticles from contacting each other and also act as a matrix in which the volume fraction of TiO_2 nanoparticles can be changed by varying the ratio between the nanoparticle size and shell thickness.

RESULTS AND DISCUSSION

Plasma-condensation-type cluster-deposition systems have been used to produce highly monodisperse metal and alloy nanoparticles of sizes varying from a few tens to several thousands of atoms using an inert-gas condensation principle.[29−32] In our system, shown schematically in Figure 1, an atomic metal vapor produced using a plasma-sputtering process, for example Ti in the present study, is condensed in a cooled inert-gas ambient at a pressure of about 5×10^{-1} Torr. The Ti atoms lose kinetic energy through successive interatomic collisions with the inert-gas atoms, leading by aggregation to Ti nanoparticles. We have produced TiO_x nanoparticles with different stoichiometries such as TiO and TiO_2 by well-controlled mixing of oxygen into the gas-aggregation region (for details, see the Experimental Methods section).

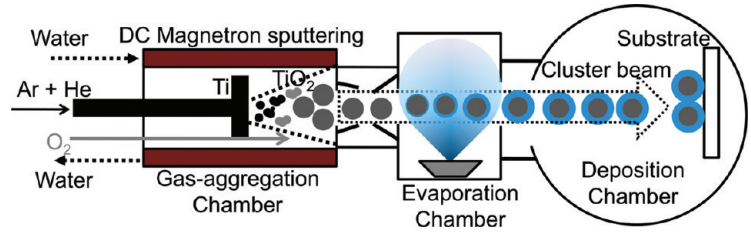

Figure 1. A schematic diagram of the cluster-deposition apparatus used for the growth of TiO_2 and TiO_2−paraffin core−shell nanoparticles.

TiO_2 nanoparticles were chosen to be coated with paraffin nanoshells for fabricating capacitors because of their higher dielectric constant. Since TiO_2 nanoparticles were extracted from the gas-aggregation chamber as a collimated beam moving toward the deposition chamber kept at a pressure of about 5×10^{-4} Torr, it was possible to coat the particles with paraffin as they pass through the evaporation chamber. This hybrid experimental method can be adapted easily to produce core−shell nanoparticles of other complex oxides and a wide range of functional molecules, such as VDF oligomers, which are structurally similar to paraffin.[33]

X-ray diffraction (XRD) measurements of pure TiO_x nanoparticles without paraffin coating prepared at various oxygen flow rates are shown in Figure 2a. Without oxygen feeding into the gas-aggregation chamber, the sputtered titanium atoms aggregate to form pure Ti

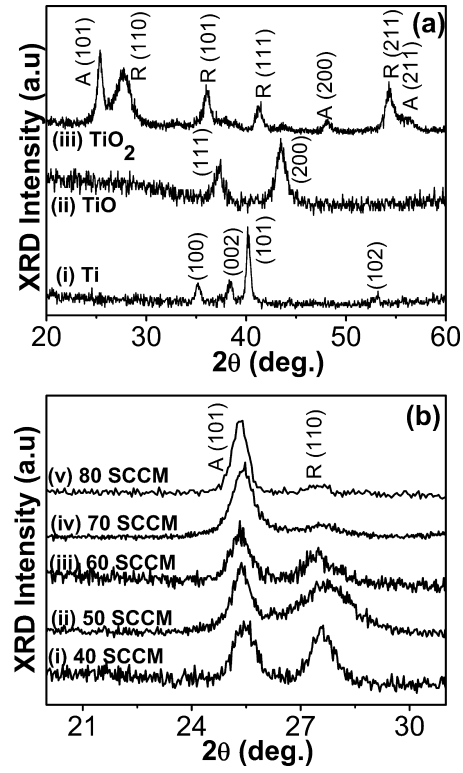

Figure 2. (a) X-ray diffractograms of uncoated TiO_x nanoparticles prepared at various oxygen flow rates: (i) 0 SCCM, (ii) 6.7 SCCM, and (iii) 50 SCCM, where SCCM denotes standard cubic centimeter per min. (b) X-ray diffractograms of TiO_2 nanoparticles prepared at oxygen flow rates of ≥40 SCCM showing the dependence of anatase and rutile phases on oxygen flow rates.

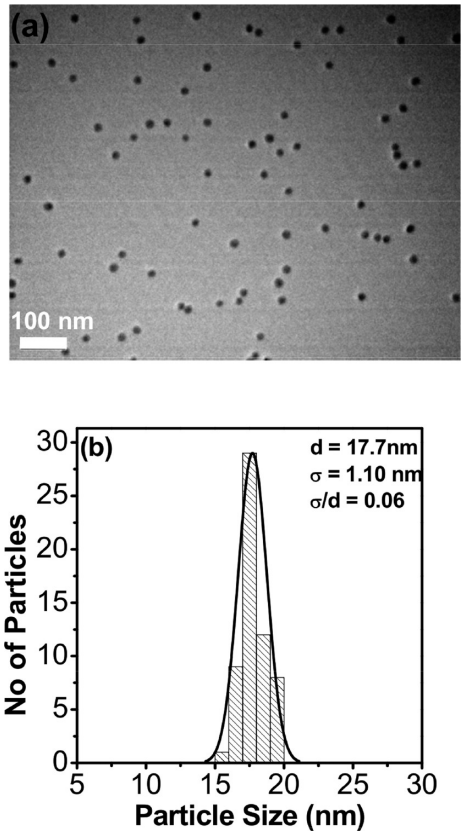

Figure 3. (a) TEM image and (b) the corresponding particle-size histogram of Ti nanoparticles, where σ and *d* are standard deviation and average particle size, respectively. A small value of σ/*d* = 0.06 reveals the narrow size-distribution of nanoparticles.

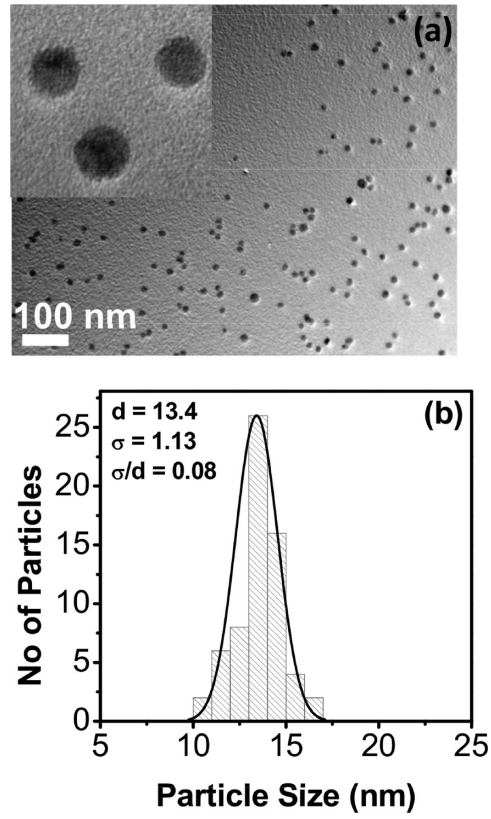

Figure 4. (a) TEM image and (b) the corresponding particle-size histogram of TiO_2 nanoparticles prepared at an oxygen flow rate of 50 SCCM (standard cubic centimeter per min), where σ and *d* are standard deviation and average particle size, respectively. The TEM image of TiO_2 nanoparticles recorded at higher magnification revealing a clean surface and spherical shape is shown as the inset of panel a.

nanoparticles having the hexagonal structure (curve i in Figure 2a). At low oxygen flow rates of ≤25 SCCM (standard cubic centimeter per minute), Ti clusters oxidize to form TiO nanoparticles having the rock-salt structure as shown in the X-ray diffractogram of TiO_x clusters prepared at an oxygen flow rate 6.7 SCCM (curve ii in Figure 2a). At higher oxygen flow rates of ≥40 SCCM, the Ti clusters oxidize to form tetragonal TiO_2 nanoparticles having predominantly anatase (A) and rutile (R) structures, as shown in the X-ray diffractogram of TiO_x nanoparticles prepared at an oxygen flow rate of 50 SCCM (curve iii in Figure 2a). XRD studies clearly reveal the formation of TiO nanoparticles at low oxygen flow rates (≤25 SCCM) and TiO_2 nanoparticles at higher oxygen flow rates (≥40 SCCM). In addition, the XRD intensity of the anatase peak increases with an increase in the oxygen flow rates at above 40 SCCM and completely dominates over the rutile peak at an oxygen flow rate of 80 SCCM as shown in Figure 2b.

The average particle size, shape, and size-distribution of TiO_x nanoparticles were investigated using a transmission electron microscope (TEM). TEM micrograph (Figure 3a) and particle-size histogram (Figure 3b) of Ti nanoparticles prepared without oxygen feeding show an average particle size (*d*) of 17.7 nm with a σ/*d* = 0.06, where σ is the standard deviation.

On the other hand, TiO_2 nanoparticles prepared at an oxygen flow rate of 50 SCCM were observed to have a reduced *d* of 13.4 nm with a σ/*d* = 0.08 as shown in the TEM micrograph (Figure 4a) and particle-size histogram (Figure 4b). Similarly, the TEM micrograph and histogram of TiO nanoparticles prepared at an oxygen flow rate of 6.7 SCCM also show a reduced particle size of 15.1 nm (see the Supporting Information). These results indicate that the feeding of oxygen into the cluster-aggregation chamber also controls the size of the nanoparticles, in addition to the phase and structure. As already mentioned, the sputtered Ti atoms lose kinetic energy through successive interatomic collisions with the inert-gas atoms to reach thermal equilibrium and this process leads to an aggregation, resulting in Ti nanoparticles. On the other hand, the oxidation process upon oxygen feeding into the cluster-aggregation chamber utilizes a certain amount of thermal energy from the aggregating sputtering atoms, leading to their early attainment of thermal equilibrium and subsequently results in reduced size of the oxidized nanoparticles. The cluster-deposited TiO_x nanoparticles have a clean surface and spherical shape as clearly shown in the TEM micrograph of TiO_2 nanoparticles recorded at higher magnification (inset of Fig-

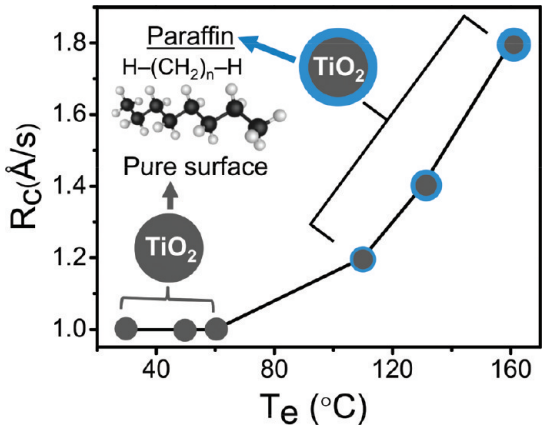

Figure 5. An increase in the deposition rate of TiO_2 nanoparticles (R_c) with an increase in the evaporation temperature of paraffin ($T_e \geq 100$ °C) due to the formation of paraffin nanoshells. At $T_e \leq 60$ °C, the surface of the TiO_2 nanoparticles seems to be pure or have thin nanoshells as evident from the observed constant R_c. The chemical structure of the paraffin nanoshells is also schematically given in the inset, where the black and gray spheres represent carbon and hydrogen atoms, respectively.

ure 4a). It is also worth noting that the observed values of $\sigma/d \leq 0.08$ in these samples reveal the monodispersion of TiO_x nanoparticles.

As mentioned above, the cluster-deposition technique has been used to produce a variety of metal and alloy nanoparticles. In a few studies, oxidation of metal clusters such as Fe and Co has been observed by exposing them to an oxygen atmosphere.[5,34] The oxidation process, however, has been observed to be size-dependent; metal clusters of a few nm in size have oxidized completely, whereas larger nanoparticles exhibited only a partial oxidation.[34] By contrast, Ti is comparatively stable against oxidation at atmospheric conditions and normally requires a very high temperature to form TiO_2 on exposure to oxygen during postdeposition treatment.[10,13] The postdeposition heat treatments, however, can lead to poor control in the particle size and size-distribution.[13] In the present study, the oxidation of Ti clusters, irrespective of their sizes, was controlled precisely by adjusting the partial pressure of oxygen in the gas-aggregation region, resulting in the growth of uniform TiO and TiO_2 nanoparticles having spherical shape. Although a pulsed microplasma cluster source has been used to grow nanocrystalline TiO_2 films by ablating atomic titanium using a pulsed jet of He and O_2, this method resulted in a broad crystallite size-distribution (2−100 nm).[35,36] As compared to the cluster-deposition method, various chemical and physical synthesis techniques require an *in situ* heating or postdeposition annealing at high temperatures of more than 400 °C to obtain anatase or rutile TiO_2 nanoparticles.[11−13] Similarly, bulk TiO is also a high temperature phase, which has been generally prepared by heating Ti with TiO_2 in vacuum at very high temperature of about 1000 °C.[37] High-temperature processing is not favorable for the formation of core−shell nanoparticles, especially in the case of paraffin or other organic nanoshells due to their low melting points and low decomposition temperatures.[28] The room temperature growth of TiO_2 nanoparticles in the present study also facilitates *in situ* deposition of paraffin nanoshells using thermal evaporation.

In the present study, TiO_2 nanoparticles having an average particle size of 13.4 nm were coated with the paraffin nanoshells. The thickness of the nanoshells was controlled precisely by varying the evaporation rate of paraffin (R_p). R_p was observed to show an increasing trend with an increase in the evaporation temperature (T_e). For example, with the cluster beam off, we measured R_p at different T_e by placing a quartz crystal thickness monitor above the evaporation source and directly in the path of the cluster beam. The distance between the evaporation source and cluster beam was about 4 cm. At a working pressure of about 5×10^{-4} Torr, the paraffin was observed to evaporate with an R_p of 0.09 nm/s at 60 °C. R_p reaches to 7 nm/s at 100 °C and increases rapidly upon further increase in T_e. With both the cluster beam and thermal evaporation of paraffin on, we measured the deposition rate of TiO_2 nanoparticles (R_c) by placing the quartz crystal thickness monitor at the exact position where the substrates were kept during the sample preparation. When TiO_2 nano-

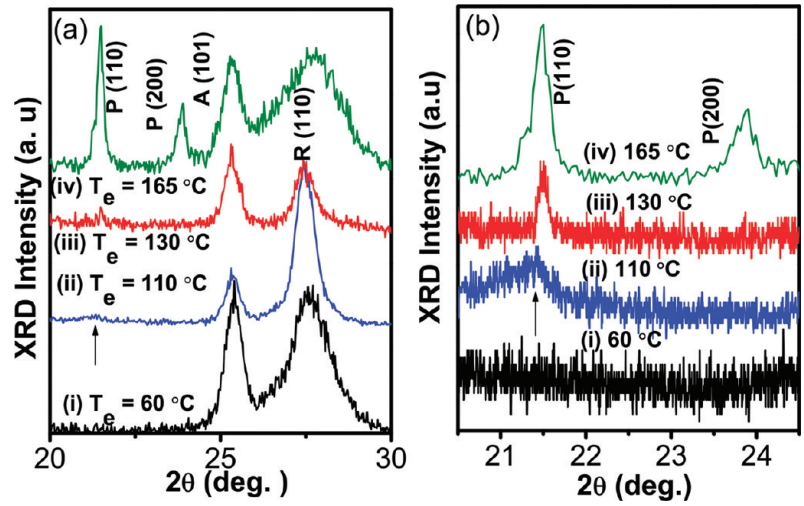

Figure 6. (a) X-ray diffractograms of TiO_2−paraffin core−shell nanoparticles prepared at different T_e (measured with a scan speed of 3 s for each data point at an interval of 0.03°); (b) the corresponding X-ray diffractograms of TiO_2−paraffin core−shell nanoparticles measured with a very slow scan speed of 6 s for each data point at an interval of 0.004° from $2\theta = 20.5°-24.5°$.

particles passed through the evaporation chamber, paraffin was directly deposited on their surface to form nanoshells, resulting in an increase in R_c as shown in Figure 5. At $T_e = 60$ °C, R_c does not show any increase as compared to that of uncoated nanoparticles, probably due to a very thin nanoshell coating. A considerable increase in R_c, however, was observed with increasing T_e above 100 °C due to an increase in the thickness of the paraffin nanoshells.

X-ray diffraction measurements of TiO_2−paraffin core−shell nanoparticles measured at 2θ ranging from 20° to 30° are shown in Figure 6a, where θ is the incident angle of the X-rays. To detect the low-intensity diffraction peaks corresponding to a very thin coating of paraffin, X-ray diffractograms of TiO_2−paraffin core−shell nanoparticles were measured at a very slow scan rate in the 2θ range of 20.5° to 24.5° (see Figure 6b). Note that the recorded X-ray diffractogram of pure paraffin was observed to show a predominant peak at $2\theta = 21.8°$ along with a comparatively weak peak at $2\theta = 24.3°$ corresponding to (110) and (200) of orthorhombic structure (not shown in the Figure 6). X-ray diffractograms of the TiO_2−paraffin core−shell nanoparticles prepared at T_e of 60 °C did not show diffraction peaks corresponding to paraffin (curve i in Figure 6a and Figure 6b) probably due to the very thin paraffin coating. On the other hand, the diffraction peaks corresponding to paraffin were visible (indicated by an arrow in curve ii in Figure 6a and Figure 6b) for core−shell nanoparticles prepared at $T_e \geq 110$ °C and become dominant in comparison with the diffraction peaks from anatase and rutile TiO_2 structures for core−shell nanoparticles prepared at $T_e = 165$ °C (curve iv in Figure 6a and Figure 6b). Therefore, these results reveal that the thickness of the paraffin shell around the TiO_2 nanoparticle core increases with an increase in the evaporation temperature of paraffin.

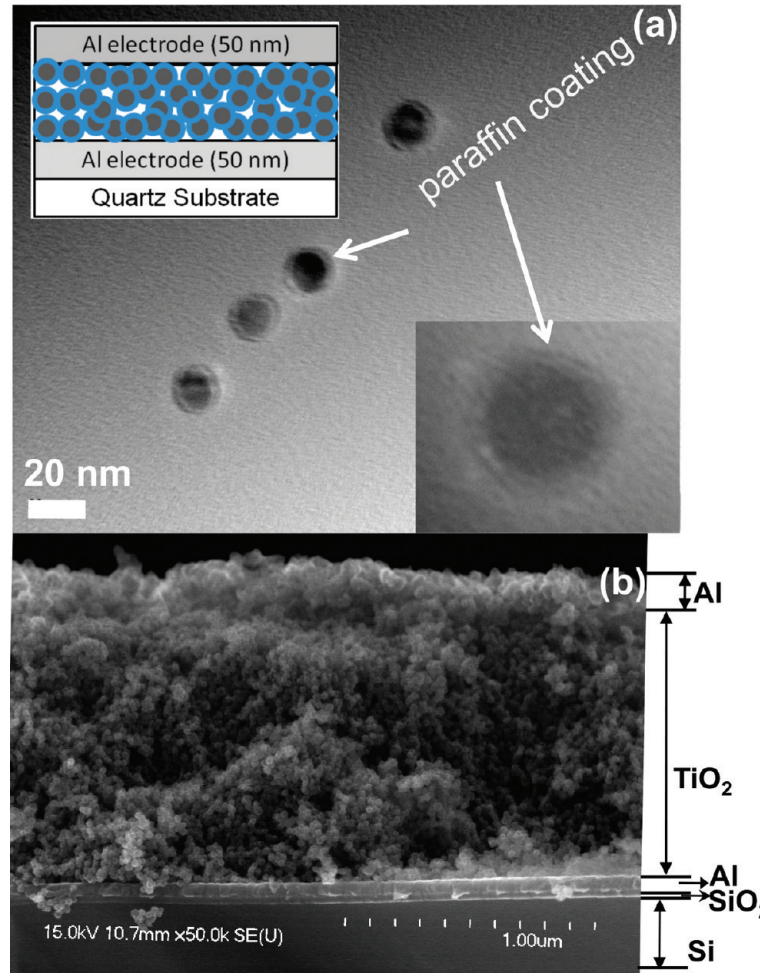

Figure 7. (a) A typical TEM image showing the TiO_2−paraffin core−shell nanoparticles prepared at $T_e = 110$ °C, where a single core−shell nanoparticle recorded at higher magnification is shown in the lower inset. A schematic diagram of a parallel-plate capacitor in which TiO_2−paraffin core−shell nanoparticle layer having thickness of 220 nm used as a dielectric is shown in the upper inset. (b) Cross-sectional FESEM image of a parallel-plate capacitor, consisting of a TiO_2 nanoparticle dielectric layer of ~1 μm thickness with a ~60 nm thick bottom and ~100 nm top aluminum electrodes, fabricated on a thin SiO_2-covered Si substrate.

The internal structure of the TiO_2−paraffin core−shell nanoparticles was probed using TEM. In an agreement with the XRD results, the paraffin-coated TiO_2 nanoparticles show a core−shell structure as shown in the TEM micrograph of TiO_2−paraffin core−shell nanoparticles prepared at $T_e = 110$ °C (Figure 7a). The TEM studies also revealed that the thickness of the paraffin nanoshell (δ) increased from 2 to 3.5 nm on increasing T_e from 110 to 165 °C. Note that formation of core−shell nanoparticles is strongly dependent on the material systems in most of the synthesis techniques. For example, in the case of bimetallic nanoparticles, a significant difference in their atomic sizes and surface energies resulted in a preferential surface segregation of the material having relatively large atomic size and low surface energy, leading to the spontaneous formation of core−shell structures.[2,3,6] However, for this study, the paraffin nanoshells were directly deposited on the surface of the TiO_2 nanoparticles in the gas phase, while they were *in-flight*. The thin coating of paraffin nanoshells separates the TiO_2 nanoparticles and prevents them from contacting each other on substrates. In addition, paraffin nanoshells act as a matrix and an increase in the coating thickness will decrease the volume fraction of TiO_2 nanoparticles.

Parallel-plate capacitors made of TiO_2−paraffin core−shell nanoparticles as dielectrics were fabricated (schematically shown in upper inset of Figure 7a for investigating their dielectric properties. Note that the film is also expected to have a certain volume fraction of voids (see upper inset of Figure 7a), which will reduce the effective dielectric constant. The presence of voids in the nanoparticle layer is clearly seen in the cross-sectional field emission scanning electron microscope

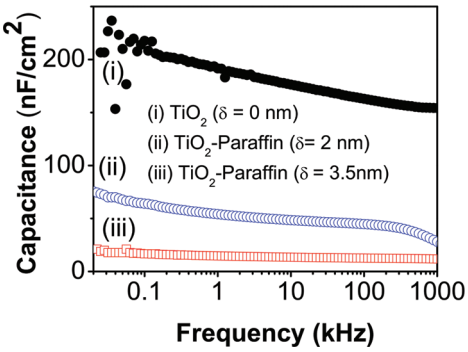

Figure 8. The frequency-dependent capacitance of the TiO_2−paraffin core−shell nanoparticle layers having different paraffin nanoshell thicknesses (δ).

(FESEM) image of a typical parallel-plate capacitor, consisting of a TiO_2 nanoparticle dielectric layer of ~1 μm thickness with a ~60 nm thick bottom and ~100 nm top aluminum electrodes, fabricated on a thin SiO_2-covered Si substrate as shown in Figure. 7b. Since the insulating quartz substrate showed a strong charging effect during the FESEM measurements, the Si substrate was used for these measurements. It is also clear from Figure 7b that the crystallites in the top aluminum film have much bigger sizes of ~40 nm as compared to TiO_2 nanoparticles (also see the Supporting Information). The frequency-dependent capacitance and dielectric loss of capacitors having TiO_2−paraffin core−shell nanoparticle films with varying δ as dielectrics are shown in Figure 8 and Figure 9, respectively. The capacitance of core−shell nanoparticles increases with a decrease in δ from 3.5 (curve iii in Figure 8) to 2.0 nm (curve ii in Figure 8) and shows higher values for pure TiO_2 nanoparticles (curve i Figure 8). This is due to an increase in the effective dielectric constant caused by an increase in the volume fraction of TiO_2 nanoparticles. The effective dielectric constant at 1 kHz estimated from the capacitance spectra for the TiO_2−paraffin core−shell nanoparticles having different δ values of 3.5, 2.0, and 0 nm are about 4, 11, and 58, respectively, where the dielectric constant of pure paraffin is about 2. Although the presence of voids is expected in the nanoparticle dielectric layer as shown in the cross-sectional FESEM image, the experimental evaluation of the void fraction in these layers is difficult because of their inhomogeneous distribution. However, a decrease in the effective dielectric constant is clearly seen in these nanoparticles. For example, the effective dielectric constant of pure TiO_2 nanoparticles decreases to 58 as compared to the bulk value of 80 due to the presence of voids.[40]

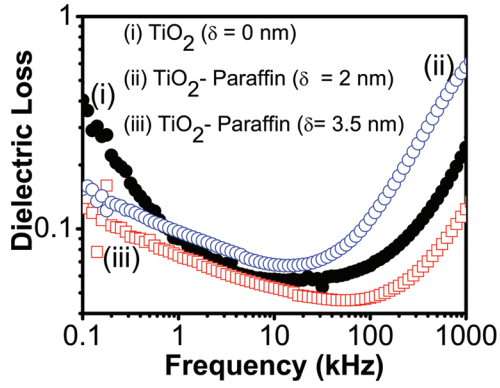

Figure 9. The frequency-dependent dielectric losses of the TiO_2−paraffin core−shell nanoparticle layers having different nanoshell thicknesses (δ).

It has been reported that the capacitance of TiO_2 thin films decreased rapidly on increasing the frequency from a few Hz to 10 kHz owing to trapped charge states and to remain nearly constant at high frequencies and this dependence of dielectric constant on the frequency is called as dielectric dispersion.[38−40] By contrast, the capacitance of the films composed of TiO_2 and TiO_2−paraffin core−shell nanoparticles shows a comparatively very small decrease in capacitance on increasing the frequency up to 1 kHz and then remains nearly constant up to 1 MHz. Figure 9 shows the frequency-dependent dielectric loss of core−shell nanoparticles with varying δ; this loss should be a minimum for potential applications. TiO_2−paraffin core−shell nanoparticle layers, for example core−shell nanoparticles having a shell thickness of 3.5 nm, show a dielectric loss varying from 0.40 to 0.06 in the frequency range 100 kHz−100 MHz (curve iii of Figure 9), which is comparable to 0.05 observed in case of oxide−polymer nanocomposites[14−18] and is far better than the dielectric loss (1 to 0.1) of polycrystalline TiO_2 films observed in this frequency range.[35−37]

CONCLUSIONS

We have used a hybrid deposition method consisting of the plasma-condensation-type cluster-deposition technique and thermal evaporation source to produce TiO_2−paraffin core−shell nanoparticles. This experimental method can be extended easily to produce core−shell nanoparticles, irrespective of material systems, from a variety of inorganic−organic or inorganic−inorganic materials with novel functional properties. Monodisperse and spherical TiO_2 nanoparticles were produced by optimizing the oxygen flow rates in the gas-aggregation chamber and were coated with uniform paraffin nanoshells, when they were *in-flight* toward the substrates. The paraffin nanoshells prevent the TiO_2 nanoparticles from contacting each other and also act as matrix. XRD and TEM results show that the thickness of the paraffin nanoshells can be controlled precisely by adjusting the evaporation temperature. Parallel-plate capacitors with TiO_2−paraffin core−shell nanoparticles with varying shell thickness as dielectric were fabricated. The effective dielectric constant of TiO_2−paraffin nanocomposites was tailored by controlling the thickness of the paraffin nanoshells. As compared to polycrystalline TiO_2 films, TiO_2−paraffin core−shell nanoparticles show low dielectric dispersion and dielectric loss in the frequency range of 100 Hz to 1 MHz.

EXPERIMENTAL METHODS

Growth of Monodisperse TiO_2 Nanoparticles. The experimental apparatus (Figure 1) consists of a cluster-formation chamber having a magnetron plasma-sputtering discharge with a gas-aggregation tube cooled using water, an evaporation chamber for coating the paraffin nanoshells on the surface of nanoparticles prior to the deposition, and a deposition chamber, where the substrates were kept at room temperature. The base pressure of all of the chambers was about 1×10^{-6} Torr. We used water to cool the gas-aggregation tube for promoting the oxide formation instead of the liquid nitrogen cooling generally used for producing metal and alloy clusters. The Ti vapor was produced from a high purity Ti target (99.99%) using DC magnetron sputtering, where argon (Ar) and helium (He) were used as sputtering gases. During deposition, the gas-aggregation chamber was maintained at about 5×10^{-1} Torr, whereas the evaporation and deposition chambers were kept at relatively low pressures of about 5×10^{-4} Torr. The sputtered Ti atoms in a cooled inert gas-ambient aggregated into Ti clusters, which were subsequently oxidized to obtain TiO_x nanoparticles with different stoichiometries and crystal structures by varying the oxygen flow rates from 6.7 to 80 SCCM (standard cubic centimeter per minute), while keeping the flow rates of Ar and He constant as 275 and 100 SCCM, respectively.

Formation of Paraffin Nanoshells. TiO_2 nanoparticles were extracted through a series of collimated apertures and skimmers as a well-focused beam toward the deposition chamber. Paraffin (melting point of *ca.* 70−80 °C, Sigma Aldrich) was evaporated using a resistively heated stainless steel crucible to coat the TiO_2 nanoparticles with paraffin nanoshells, while the nanoparticles passed through the evaporation chamber. The evaporation temperature of paraffin (T_e) was varied from 60 to 165 °C to control the thickness of the paraffin nanoshells.

Structural Characterization. Bare TiO_x and TiO_2−paraffin core−shell nanoparticles are deposited on Si substrates and carbon-coated Cu grids to investigate their structural properties using X-ray diffraction (XRD: Rigaku D/Max-B diffractometer) and transmission electron microscope [TEM: JEOL 2010 (acceleration voltage, 200 kV; resolution, ~1.94 Å; and operating pressure, ~ 10^{-9} Torr)], respectively. The complete X-ray diffraction spectra of TiO_x and TiO_2−paraffin core−shell nanoparticles from 2θ = 20° to 60° were recorded with a scan speed of 3 s for each data point at an interval of 0.03°. To detect low-intense diffraction peaks from paraffin nanoshells, a slow XRD scan with a speed of 6 s for each data point at an interval of 0.004° from 2θ = 20.5°−24.5° was performed for TiO_2−paraffin core−shell nanoparticles.

Fabrication and Characteristics of Capacitors. Parallel-plate capacitors with bare TiO_2 and TiO_2−paraffin core−shell nanoparticle layers of thickness ≈ 220 nm as dielectrics and aluminum thin films of 50 nm thickness as top and bottom electrodes were fabricated for capacitance measurements, which were made with an impedance analyzer (HP 4192A) at 0.1 V amplitude. Square-shaped Al electrodes were fabricated using vacuum thermal-evaporation of aluminum. The thicknesses of the dielectric and aluminum films were measured using quartz crystal thickness monitor. The area of the capacitors having TiO_2 and TiO_2−paraffin core−shell nanoparticle layers as dielectrics was 3 and 9 mm^2, respectively. Field-emission scanning electron microscope [FESEM: Hitachi S4700 (magnification, up to 500 000×; resolution, up to 1.2 nm) was used to record the cross-sectional view of the parallel plate capacitor. For cross-sectional FESEM measurements, we have fabricated a typical parallel-plate capacitor, consisting of a TiO_2 nanoparticle dielectric layer of ~1 μm thickness with a ~60 nm thick bottom and ~100 nm top aluminum electrodes, on a thin SiO_2-covered Si substrate.

Acknowledgment. We are grateful for the financial support to the U.S. Office of Naval Research (Grant No. N00014-06-1-0604), the US Army Research Office (Grant No. W911NF-08-1-0311), National Science Foundation−Materials Research Science and Engineering Center (Grant No. DMR-0820521), and the Nebraska Center for Materials and Nanoscience. We also would like to acknowledge Zhiquang Sun for his technical assistance.

Supporting Information Available: Supplementary figures. This material is available free of charge *via* the Internet at http://pubs.acs.org.

REFERENCES AND NOTES

1. Wang, C.; Peng, S.; Chan, R.; Sun, S. Synthesis of AuAg Alloy Nanoparticles from Core/Shell Structured Ag/Au. *Small* **2009**, *5*, 567–570.
2. Tao, F.; Grass, M. E.; Zhang, Y.; Butcher, D. B.; Renzas, J. R.; Liu, Z.; Chung, J. Y.; Mun, B. S.; Salmeron, M.; Somarjai, G. A. Reaction-Driven Restructuring of Rh−Pd and Pt−Pd Core−Shell Nanoparticles. *Science* **2006**, *2*, 932–934.
3. Kim, H. Y.; Kin, H. G.; Ryu, J. H.; Lee, H. M. Preferential Segregation of Pd Atoms in the Ag−Pd Bimetallic Cluster: Density Functional Theory and Molecular Dynamics Simulation. *Phys. Rev. B* **2007**, *75*, 212105−1212105−4.
4. Lu, A. H.; Salabas, E. L. Schüth, F. Magnetic Nanoparticles: Synthesis, Protection, Functionalization, and Application. *Angew. Chem., Int. Ed.* **2007**, *46*, 1222–1244.
5. Wei, X.-H.; Skomski, R.; Sun, Z.-G.; Sellmyer, D. J. Proteresis in Co:CoO Core−Shell Nanoclusters. *J. Appl. Phys.* **2008**, *103*, 07D514−1-07D514−4.
6. Cheng, D.; Wang, W.; Huang, S. Core−Shell Structured Bimetallic Clusters and Nanowires. *J. Phys.: Condens. Matter* **2007**, *19*, 356217−1356217−12.
7. Das, B. C.; Pal, A. J. Core−Shell Nanoparticles with Functionalized Quantum Dots and Ionic Dyes: Growth, Monolayer Formation, and Electrical Bistabilty. *ACS Nano* **2009**, *21*, 5292–5299.
8. Guchhait, A; Rath, A. K.; Pal, A. J. Hybrid Core−Shell Nanoparticles: Photoinduced Electron-Transfer for Charge Separation and Solar Cell Applications. *Chem. Mater.* **2008**, *2*, 1930–1938.
9. Skaff, H; Sill, K; Emrick, T. Quantum Dots Tailored with Poly(para-phenylene vinylene). *J. Am. Chem. Soc.* **2004**, *126*, 11322–11325.
10. Burns, G. P. Titanium Dioxide Dielectric Films Formed by Rapid Thermal Oxidation. *J. Appl. Phys.* **1988**, *65*, 2095–2097.
11. Tang, J.; Redl, F.; Zhu, Y.; Siegrist, T.; Brus, L. E.; Steigerwald, M. T. An Organometallic Synthesis of TiO_2 Nanoparticles. *Nano Lett.* **2005**, *5*, 543–548.
12. Biener, J.; Farfan-Arriba, E.; Biener, M.; Friend, C. M.; Madix, R. J. Synthesis of TiO_2 Nanoparticles on the Au (111) Surface. *J. Chem. Phys.* **2005**, *123*, 094705-1−094705-6.
13. Mialon, G; Gohin, M; Gacoin, Boilot, J. P. High Temperature Strategy for Oxide Nanoparticle Synthesis. *ACS Nano* **2008**, *2*, 2505–2512.
14. Arbatti, M.; Shan, X.; Cheng, Z.-Y. Ceramic-Polymer Composites with High Dielectric Constant. *Adv. Mater.* **2007**, *19*, 1369–1372.
15. Li, J.; Seok, S.; Chu, B.; Dogan, F.; Zhang, Q.; Wang, Q. Nanocomposites of Ferroelectric Polymers with TiO_2 Nanoparticles Exhibiting Significantly Enhanced Electrical Energy Density. *Adv. Mater.* **2009**, *21*, 217–221.
16. Li, J.; Claude, J.; Norena-Franco, L. E.; Seok, S.; Wang, Q. Electrical Energy Storage in Ferroelectric Polymer Nanocomposites Containing Surface-Functionalized $BaTiO_2$ Nanoparticles. *Chem. Mater.* **2008**, *20*, 6304–6306.
17. Kim, P.; Jones, S. C.; Hotchkiss, P. J.; Hotchkiss, J. N.; Haddock, J. N.; Kippelen, B. Phosphonic Acid-Modified Barium Titanate Polymer Nanocomposites with High Permittivity and Dielectric Strength. *Adv. Mater.* **2007**, *19*, 1001–1005.
18. Kim, P.; Doss, N. M.; Tillotson, J. P.; Hotchkiss, P. J.; Pan, M.-J.; Marder, S. R.; Li, J.; Calame, J. P.; Perry, J. W. High Energy Density Nanocomposites Based on Surface-Modified $BaTiO_3$ and a Ferroelectric Polymer. *ACS Nano* **2009**, *3*, 2581–2592.
19. Li, J. Y.; Zhang, L.; Ducharme, S. Electric Energy Density of Dielectric Nanocomposites. *Appl. Phys. Lett.* **2007**, *90*, 132901−1132901−3.
20. Li, J. Exchange Coupling in P(VDF-TrFE) Copolymer Based All-Organic Composites with Giant Electrostriction. *Phys. Rev. Lett.* **2003**, *90*, 217601-1–217601-4.

21. Harden, E.; Ploumen, S.; Fricke, B.; Miller, T.; Snyder, K. Energy Storage Devices for Future Hybrid Electric Vehicles. *J. Power Sources.* **2007**, *168*, 2–11.
22. Sarjeant, W. J.; Clelland, I. W.; Price, R. A. Capacitive Components for Power Electronics. *Proc. IEEE* **2001**, *89*, 846–855.
23. Simon, P.; Gogotsi, Y. Materials for Electrochemical Capacitors. *Nat. Mater.* **2008**, *7*, 845–854.
24. Jayalakshmi, M.; Balakrishnan, K. Simple Capacitors to Supercapacitors—A Overview. *Int. J. Electrochem. Sci.* **2008**, *3*, 1196–1217.
25. Cheng, Z.-Y.; Zhang, Q. M.; Bateman, F. B. Dielectric Relaxation Behavior and Its Relation to Microstructure in Relaxor Ferroelectric Polymers: High Energy Electron Irradiated Poly(vinylidene fluoride-trifluoroethylene) Copolymers. *J. Appl. Phys.* **2002**, *92*, 6749–6755.
26. Huang, C.; Zhang, Q. M.; Su, J. High-Dielectric-Constant All-Polymer Percolative Composites. *Appl. Phys. Lett.* **2003**, *82*, 3502–3504.
27. Chu, B.; Zhou, X.; Ren, K.; Neese, B.; Lin, M.; Wang, Q.; Baurer, F.; Zhang, Q. M. A Dielectric Polymer with High Electric Energy Density and Fast Discharge Speed. *Science* **2006**, *313*, 334–336.
28. Bruice, P. Y. *Organic Chemistry*; Prentice-Hall: NJ, 2001.
29. Haberland, H.; Mall, M.; Moseler, M.; Qiang, Y.; Reiners, Thurner, Y. J. Filling of Micron-Sized Contact Holes with Copper by Energetic Cluster Impact. *J. Vac. Sci. Technol., A* **1994**, *12*, 2925–2930.
30. Meldrim, J. M.; Qiang, Y.; Liu, Y.; Haberland, H.; Sellmyer, D. J. Magnetic Properties of Cluster-Beam-Synthesized Cobalt: Noble-Metal Films. *J. Appl. Phys.* **2000**, *87*, 7013–7015.
31. Sellmyer, D. J.; Luo, C. P.; Qiang, Y.; Liu, J. P. Magnetism of Nanophase Composite Films. In *Handbook of Thin Films*; Nalwa, H. S., Ed.; Academic: New York, 2002, pp 337−374.
32. Peng, D. L.; Yamada, H.; Hihara, T.; Uchida, T.; Sumiyama, K. Dense Fe Cluster-Assembled Films by Energetic Cluster Deposition. *Appl. Phys. Lett.* **2004**, *85*, 2935–2937.
33. Noda, K.; Ishida, K.; Horiuchi, T.; Matsushige, K.; Kubono, A. Structures of Vinylidene Fluoride Oligomer Thin Films on Alkali Halide Substrate. *J. Appl. Phys.* **1999**, *86*, 3688–3693.
34. Qiang, Y.; Antony, J.; Sharma, A.; Nutting, J.; Sikes, D.; Meyer, D. Iron/iron Oxide Core-Shell Nanoclusters for Biomedical Applications. *J. Nanopart. Res.* **2006**, *8*, 489–496.
35. Ducati, C.; Barborini, E.; Bongirono, G.; Vinati, S.; Milani, P.; Midgley, P. A. Titanium Fullerenoid Oxides. *Appl. Phys. Lett.* **2005**, *87*, 201906-1–201906-3.
36. Barborini, E.; Ducati, C.; Bottani, C. E.; Milani, P. Engineering the Nanocrystalline Structure of TiO_2 Films by Aerodynamically Filtered Cluster Deposition. *Appl. Phys. Lett.* **2002**, *81*, 3052–3054.
37. Valeeva, A. A.; Rempel, A. A.; Sprengel, W.; Schaefer, H.-E. Vacancies on the Ti Sublattice in Titanium Monoxide TiO_y Studied using Positron Annihilation Techniques. *Phys. Rev. B* **2007**, *75*, 094107-1−094107-6.
38. Stamate, M. D. Dielectric Properties of TiO_2 Thin Films Deposited by a DC Magnetron Sputtering System. *Thin Solid Films* **2000**, *372*, 246–249.
39. Karunagaran, B.; Chung, S. J.; Suh, E.-K.; Mangalaraj, D. Dielectric and Transport Properties of Magnetron Sputtered Titanium Dioxide Thin Films. *Phys. B* **2005**, *239*, 129–134.
40. Bessergenev, V. High-Temperature Anomalies of Dielectric Constant in TiO_2 Thin Films. *Mater. Res. Bull.* **2009**, *44*, 1722–1728.